

On the value of corner reflectors and surface models in InSAR precise point positioning

Yang, Mengshi; Lopez Dekker, Paco; Dheenathayalan, Prabu; Liao, Mingsheng; Hanssen, Ramon

DOI

[10.1016/j.isprsjprs.2019.10.006](https://doi.org/10.1016/j.isprsjprs.2019.10.006)

Publication date

2019

Document Version

Accepted author manuscript

Published in

ISPRS Journal of Photogrammetry and Remote Sensing

Citation (APA)

Yang, M., Lopez Dekker, P., Dheenathayalan, P., Liao, M., & Hanssen, R. (2019). On the value of corner reflectors and surface models in InSAR precise point positioning. *ISPRS Journal of Photogrammetry and Remote Sensing*, 158, 113-122. <https://doi.org/10.1016/j.isprsjprs.2019.10.006>

Important note

To cite this publication, please use the final published version (if applicable). Please check the document version above.

Copyright

Other than for strictly personal use, it is not permitted to download, forward or distribute the text or part of it, without the consent of the author(s) and/or copyright holder(s), unless the work is under an open content license such as Creative Commons.

Takedown policy

Please contact us and provide details if you believe this document breaches copyrights. We will remove access to the work immediately and investigate your claim.

On the value of corner reflectors and surface models in InSAR precise point positioning

Mengshi Yang^{a,b}, Paco López-Dekker^a, Prabu Dheenathayalan^a, Mingsheng Liao^{b,*}, Ramon F. Hanssen^a

^aDepartment of Geoscience and Remote Sensing, Delft University of Technology, 2628CN Delft, The Netherlands

^bState Key Laboratory of Information Engineering in Surveying, Mapping and Remote Sensing, Wuhan University, Wuhan 430079, China

Abstract

To correctly interpret the estimated displacements in InSAR point clouds, especially in the built environment, these need to be linked to real-world structures. This requires the accurate and precise 3D positioning of each point. Artificial ground control points (GCPs), such as corner reflectors, serve this purpose, but since they require efforts and resources, there is a need for criteria to assess their usefulness. Here we evaluate the value and necessity of using GCPs for different scenarios, concerning the required efforts, and compare this to alternatives such as digital surface models (DSM) and advanced (geo) physical corrections. We consider single-epoch as well as multi-epoch GCP deployment, reflect on the number of GCPs required in relation to the number of SAR data acquisitions, and compare this with digital surface models of different quality levels. Analyzing the geolocation performance using TerraSAR-X and Sentinel-1 data, we evaluate the pros and cons of various deployment options and show that the multi-epoch deployment of a GCP yields optimal geolocalization results in terms of precision, accuracy, and reliability.

Keywords: SAR; Persistent scatterer; Geolocalization; Corner reflector; LiDAR DSM; Synthetic aperture radar interferometry

1. Introduction

Persistent scatterer interferometry (PSI) is an advanced Interferometric Synthetic Aperture Radar (InSAR) technique for mapping the displacement of geo-objects, i.e., the Earth's surface itself or objects on it. PSI exploits coherent points—the persistent scatterers (PS)—in time series of SAR images and estimates their differences in line-of-sight range over time. Together, these coherent points form a PS point cloud. Compared to the millimeter-level precision

for the estimated relative displacements, the positioning precision and accuracy of PS in a 3D datum is in the range of meters, particularly in the cross-range direction (Gernhardt et al., 2015; Dheenathayalan et al., 2016). This hampers the interpretation of the results, particularly in a complex urban environment, as the PS are typically not exactly positioned on the object that is causing the reflection. To explore the full potential of PSI, PS point positioning must be optimized.

Lately, significant progress has been made in improving the 2D radar coordinate accuracy in an absolute sense, see Small et al. (2004); Schubert et al. (2010); Eineder et al. (2011); Cong et al. (2012); Schubert et al. (2015); Balss et al. (2018). These methods involve corrections of secondary positioning components including azimuth shifting, atmospheric path delay, plate motion, solid Earth tide, and polar motion, such methods can be collectively referred to

☆

E-mail addresses: M.Yang@tudelft.nl (M. Yang),
F.LopezDekker@tudelft.nl (P.López-Dekker),
P.Dheenathayalan@tudelft.nl (P.Dheenathayalan),
Liao@whu.edu.cn (M.Liao),
R.F.Hanssen@tudelft.nl (R.F.Hanssen).

*Corresponding author

Preprint submitted to *ISPRS Journal of Photogrammetry and Remote Sensing*

October 22, 2019

as the geophysical method. Yet, while this improves the absolute range and azimuth position in *radar* coordinates, it does not yield an estimate for the cross-range position, which is essential for practical 3D *geographic* positioning.

Full 3D geometric fusion methods, see Gernhardt et al. (2012); Gisinger et al. (2015); Duque et al. (2016); Zhu et al. (2016); Montazeri et al. (2018), require the identification of physically identical scatterers visible in opposing imaging geometries, e.g., lamp posts, and are therefore strongly depending on such targets-of-opportunity (ToO). For medium/low-resolution SAR data, finding such ToO in opposite tracks is very difficult. Considering Sentinel-1 data, there are no reports in literature concerning the 3D positioning accuracy.

For (In) SAR, artificial ground control points (GCPs) are typically corner reflectors (CR) or transponders. CRs are used for external radiometric calibration of SAR systems (van Zyl, 1990; Sarabandi & Chiu, 1996; Small et al., 2007; Shimada et al., 2009), deformation measurements in low coherence areas (Hanssen, 2001; Xia et al., 2002; Crosetto et al., 2016), accuracy assessment of InSAR measurements (Ferretti et al., 2007; Marinkovic et al., 2008; Garthwaite, 2017), and to calibrate sensor timing offsets (Small et al., 2004, 2007; Miranda et al., 2013).

CRs have a high and stable radar cross section (RCS), a well-defined scattering center (the apex), and are easily identified in the image. However, while precise geolocation with the aid of GCPs is common in the field of photogrammetry, the value of 3D geolocation of entire PSI point clouds using GCPs has not yet been discussed, to the authors' knowledge.

Ideally, the philosophy of remote sensing is to avoid installing GCPs in the terrain, as it involves extra cost and effort for manufacturing, deployment, and maintenance, it requires physical access to the area, and it is very sensitive to disturbance. Moreover, it requires additional geodetic measurements to obtain ground truth in position and/or changes in position. Therefore, there is a strong incentive to find alternative methods to achieve the same objectives.

Here we assess when it makes sense to deploy GCPs, which alternatives are available, and how these compare to the use of installed GCPs. Moreover, we review the strategy of deployment, i.e., what are the

minimum requirements for the (i) number, (ii) the type, and (iii) the location of the GCPs, (iv) the duration of deployment, (v) the conditions for the additional collocated geodetic measurements, (vi) the required effort in terms of cost and resources, and (vii) an evaluation with potential alternative approaches avoiding the GCP deployment, such as using targets-of-opportunity.

A high-resolution Digital Surface Model (DSM) can also be counted as a target-of-opportunity, with thousands of virtual GCPs, and may be a valid alternative for using artificial GCPs.

This paper is structured as follows. Section 2 reviews the principles of scatterer geolocation and the corresponding error factors. Section 3 describes the geolocation methods assisted by GCPs and section 4 introduces the geolocation method assisted by DSMs. The experimental setup is given in section 5, and results of TerraSAR-X and Sentinel-1 data are given in section 6.1 and section 6.2. Section 6.3 discusses the influence of different types of DSMs on positioning precision. A comparison of the corrections methods is given Section 7 and conclusions are drawn in section 8.

2. Point scatterer geolocation

The geolocation process references a pixel in SAR geometry onto a geodetic datum. It describes the conversion of azimuth line and range pixel position of a scatterer in the 2D image to a 3D coordinate system (Schreier, 1993; Zhang et al., 2012). Given radar timing annotations, including the time of the first range sample, $t_{r,0}$, range sampling rate (RSR), pulse repetition frequency (PRF) and the state vectors describing the trajectory of a satellite during the time of data acquisition, a point at position T on the Earth's surface can be located by solving the Range-Doppler-Ellipsoid/DEM equations.

2.1. Transformation to 3D coordinate system

Fig. 1 illustrates the positioning procedure from a scatterer T at line and pixel coordinate (l_T, p_T) in the radar image to its corresponding position (x_T, y_T, z_T) in a 3D Terrestrial Reference Frame (TRF) realizing an Earth-Centered-Earth-Fixed (ECEF) reference system (Schreier, 1993).

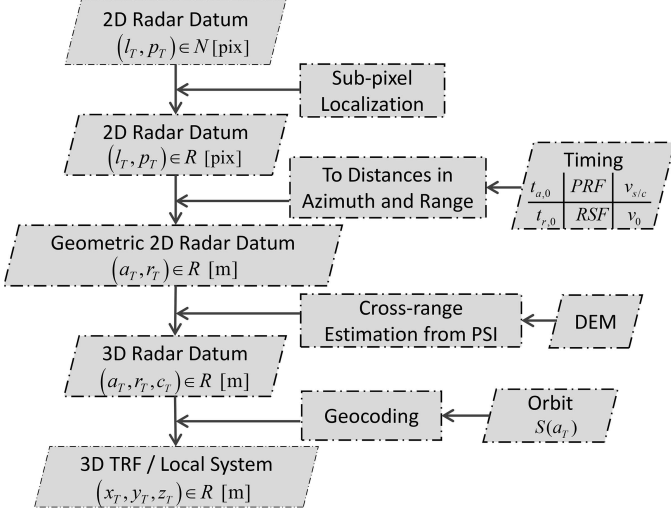


Figure 1: Methodology of point scatterer positioning.

The sub-pixel position of the effective phase center T within a resolution cell (l_T, p_T) is determined through sinc-interpolations. The variance of localization of a scatterer T in azimuth $\sigma_{l_T}^2$ and range $\sigma_{p_T}^2$ direction is given by (Bamler & Eineder, 2005)

$$\sigma_{l_T}^2 = \sigma_{p_T}^2 = \frac{3}{2 \cdot \pi^2 \cdot \text{SCR}}, \quad (1)$$

where SCR is the Signal to Clutter Ratio of a point. Eq. (1) is the Cramer-Rao bound for a change of the peak due to clutter (Stein, 1981; Bamler & Eineder, 2005), under the assumption of homogeneous area and circularly Gaussian clutter.

The sub-pixel image position can be transformed to 2D geometric radar coordinates with the PRF, $t_{r,0}$, RSR, the velocity of ground track $v_{g/t}$, and the speed of light v_0 . The origin of the radar coordinate system is the phase center of the antenna. Azimuth distance a_T is expressed as

$$a_T = \int_0^{l_T \Delta t} v_{g/t}(t) dt \approx \bar{v}_{g/t} \cdot (l_T \Delta t) \quad (2)$$

where $\Delta t = \text{PRF}^{-1}$. Range-distance r_T is expressed as:

$$r_T = \frac{v_0}{2} \cdot (t_{r,0} + p_T \Delta \tau), \quad (3)$$

where $\Delta \tau = \text{RSR}^{-1}$.

The cross-range distance ('elevation') of a point is estimated from at least one interferometric SAR observation as

$$\hat{c}_T \approx c_0 + \frac{\lambda}{4\pi} \frac{r_T}{B_\perp} \hat{\phi}_T, \quad (4)$$

where c_0 is the cross-range (elevation) of a reference point, which is assumed to be known, see section 3.2. The λ is the wavelength, B_\perp is the perpendicular baseline of the interferometric pair, and $\hat{\phi}_T$ is the estimated unwrapped topographic phase relative to the reference point. Note that the assumption of a 'known' reference point position is rarely satisfied in practice.

The cross-range c_T together with azimuth a_T , and range r_T complements the 3D orthogonal radar coordinate system. The corresponding position of point scatterer T , with state vector $\mathbf{T} = [x_T, y_T, z_T]$ in a 3D TRF, is estimated using the Range-Doppler-Ellipsoid equations see Fig. 2.

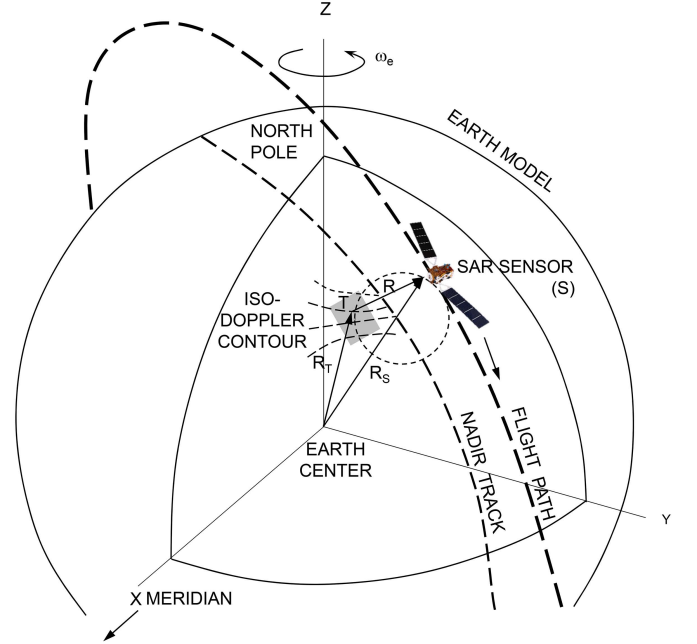


Figure 2: Earth model with an ECEF reference system, satellite and target positions. The geolocation procedure intersects R with the earth model surface and the appropriate iso-Doppler contour for scatterer T . Adapted from Olmsted (1993).

For *range*, the geometric distance r_T from scatterer T to satellite $\mathbf{S}(t_a)$ is a function of the satellite state vectors and scatterer state vector,

$$\|\mathbf{S}(t_a) - \mathbf{T}\| - r_T^2 = 0, \quad (5)$$

where $\mathbf{S}(t_a)$ is the satellite state vectors at the zero Doppler time of imaging target $t_a = l_T \Delta t$.

For *Doppler*, the scatterer T is viewed perpendicular to the orbit, i.e.,

$$f_D(t_a) + \frac{2}{\lambda} \frac{(\mathbf{S}(t_a) - \mathbf{T}) \cdot \mathbf{V}(t_a)}{\|\mathbf{S}(t_a) - \mathbf{T}\|} = 0, \quad (6)$$

where $\mathbf{V}(t_a)$ is the velocity vector of the satellite at the instant of imaging target T , and $f_D(t_a)$ is the Doppler frequency of scatterer T at azimuth position a_T .

Finally, for the *ellipsoid*, T has a vertical elevation $H(c_T)$ above a reference ellipsoid with semi-major and semi-minor axis m and f , respectively, hence

$$\frac{x_T^2}{(m + H(c_T))^2} + \frac{y_T^2}{(m + H(c_T))^2} + \frac{z_T^2}{(f + H(c_T))^2} - 1 = 0. \quad (7)$$

$H(c_T)$ is calculated from the cross-range position:

$$H(c_T) = c_T \cdot \sin \theta_{\text{inc},T} \quad (8)$$

where $\theta_{\text{inc},T}$ is the incidence angle at T . Optionally, the 3D TRF coordinates can be further transformed into a national/local coordinate system.

From Eqs. (5)–(7), the precise 3D geolocation relies on the precision of azimuth coordinate a_T , range coordinate r_T , the estimated cross-range \hat{c}_T , and the satellite orbit vectors.

2.2. Refinement in azimuth, range, and elevation

The measurements in range and azimuth are affected by additional time-variable positioning components that can range from centimeters to several meters. Due to the instrumental timing error $t_{a,\text{sysm}}$, azimuth shift $a_{\text{shift},T}$, tectonic plate movement $a_{\text{tect},T}$, and solid earth tides (SET) $a_{\text{set},T}$, the azimuth measurements of Eq. (2) can be written as

$$a_T = v_{g/t} \cdot (l_T \Delta t + t_{a,\text{sysm}}) + a_{\text{shift},T} + a_{\text{tect},T} + a_{\text{set},T}. \quad (9)$$

Similarly, the range in Eq.(3) can be expressed as:

$$r_T = \frac{v_0}{2} \cdot (t_{r,0} + p_T \Delta \tau + t_{r,\text{sysm}}) + r_{\text{apd},T} + r_{\text{tect},T} + r_{\text{set},T}, \quad (10)$$

where $t_{r,\text{sysm}}$ is the internal system delay, and $r_{\text{apd},T}$, $r_{\text{tect},T}$, and $r_{\text{set},T}$ are atmosphere path delay (APD), tectonic plate movement, and SET impacts on the range measurement, respectively (Dheenathayalan et al., 2016). Combining the equations, the error terms in azimuth and range can be expressed as:

$$\Delta a_T = v_{g/t} \cdot t_{a,\text{sysm}} + a_{\text{shift},T} + a_{\text{tect},T} + a_{\text{set},T}, \quad (11)$$

and

$$\Delta r_T = \frac{v_0}{2} t_{r,\text{sysm}} + r_{\text{apd},T} + r_{\text{tect},T} + r_{\text{set},T}, \quad (12)$$

where Δa_T and Δr_T describe the contributions in azimuth and range that need to be accounted for. Moreover, the bias due to the reference elevation needs to be accounted for.

The elevation of scatterer T is relative to a reference point. This implies that the uncertainty of the reference elevation will introduce a bias to all PS points. This elevation offset Δc is constant for all PS and affects the geographic position both in the horizontal and vertical direction. The error contributions in azimuth, range, and elevation would transmit to 3D geolocations which have to account for reaching quality geo-localization.

3. GCP-assisted InSAR precise point positioning

As discussed in the previous section, the geolocation positioning is affected by several biases. Fig. 3 illustrates that the range observation, R_{obs} , includes biases due to system-related unknowns and unaccounted geophysical effects, leading to the erroneous geolocation of the target T at position T' .

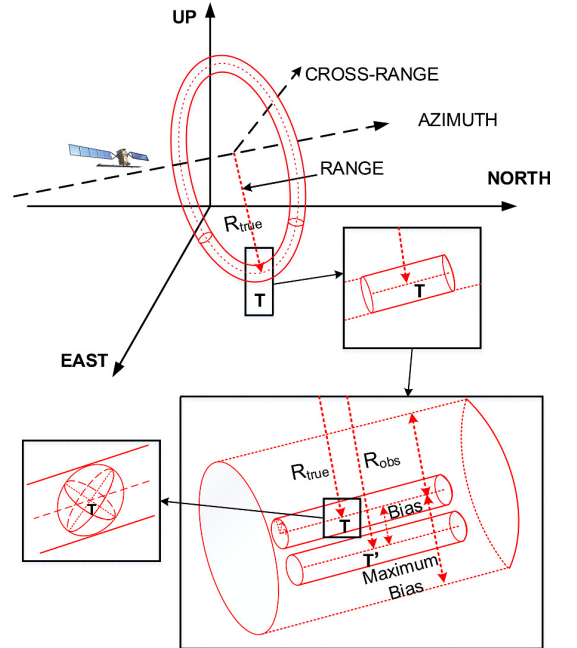


Figure 3: Positioning uncertainty cylinder of Target T . R_{true} is the range distance to the true position of T , R_{obs} is the observed range distance to the measured position of T' , the distances from T to T' is bias, the maximum bias is radius of the cylinder, the noise term in azimuth, range, cross-range formed the uncertainty ellipsoid.

The estimated range can be expressed as:

$$R_{\text{obs}} = R_{\text{true}} + R_{\text{bias}} + R_{\text{noise}}, \quad (13)$$

where R_{noise} is the zero-mean random perturbation of the estimated position, and R_{bias} is the systematic term that we are aiming to correct. The bias term is caused by system-introduced delays or unaccounted geophysical path delays. The noise includes the contributions that are system-related, geophysical, and processing-related. Assuming that this bias is constant for a relatively small scene, the positions of the targets can be corrected for by using one or more GCPs. Reducing the bias means shrinking the positioning uncertainty cylinder, to move the error ellipsoid to the true position.

In the following section, we discuss two approaches to estimate the bias in azimuth, range, and cross-range using dedicated reflectors. The first approach minimizes the effort by installing a temporary ad-hoc corner reflector during only one SAR acquisition and collecting geodetic ground-truth positioning data. We refer to this approach as the *single-epoch* approach. The second approach requires more efforts and resources and involves a continuously maintained CR, referred to as the *multi-epoch* approach. Note that the benefit of using multiple CRs instead of a single CR is trivial, as it improves the precision of the calculated offsets with $1/\sqrt{N}$.

3.1. Single-epoch CR

In this method, a GCP, typically a CR, is deployed and its phase-center position is precisely measured for a single acquisition. In our case study, we determined the location of the apex of the CRs using a GNSS (Global Navigation Satellite System) measurement.

The GNSS-derived 3D position $(x_{\text{cr}}, y_{\text{cr}}, z_{\text{cr}})$ is projected onto the 2D radar coordinates, $(a_{\text{cr,g}}, r_{\text{cr,g}})$. From the SAR intensity image we obtain an independent estimation of the radar coordinates of the target $(a_{\text{cr,s}}, r_{\text{cr,s}})$. The azimuth and range offsets are subsequently estimated as

$$\Delta a = a_{\text{cr,s}} - a_{\text{cr,g}}, \quad \text{and} \quad (14)$$

$$\Delta r = r_{\text{cr,s}} - r_{\text{cr,g}}, \quad (15)$$

respectively. The estimated offsets are applied to the estimated radar coordinates of all the PS in the image.

In azimuth, the variance of the corrected offset is,

$$\sigma_{\Delta a}^2 = \sigma_{a,s}^2 + \sigma_{a,g}^2, \quad (16)$$

where $\sigma_{a,s}^2$ is the variance of the error in the sub-pixel position estimation of the target in azimuth, as given by (1), and $\sigma_{a,g}^2$ is the corresponding variance of the GNSS measurement error. with $(\sigma_{e,g}^2, \sigma_{n,g}^2, \sigma_{u,g}^2)$. representing the variance of GNSS measurement in east, north and vertical direction, the resulting variance in azimuth direction is

$$\sigma_{a,g}^2 = \sin^2 \alpha \cdot \sigma_{e,g}^2 + \cos^2 \alpha \cdot \sigma_{n,g}^2, \quad (17)$$

where α is the heading angle between the flight direction and the north direction.

In range, the variance of the error of the corrected offset is:

$$\sigma_{\Delta r}^2 = \sigma_{r,s}^2 + \sigma_{r,g}^2, \quad (18)$$

where the second term is

$$\sigma_{r,g}^2 = \sin^2 \theta \cdot (\cos^2 \alpha \cdot \sigma_{e,g}^2 + \sin^2 \alpha \cdot \sigma_{n,g}^2) + \cos^2 \theta \cdot \sigma_{u,g}^2, \quad (19)$$

with θ the incidence angle with respect to a horizontal plane.

The main limitation of the single-epoch approach is that it only corrects for the range and azimuth offset, and not for cross-range (or elevation) offset. Consequently, while the method reduces two dimensions of the solution space, which is a positioning improvement, it still leaves the actual 3D geographic position under-determined.

3.2. Multi-epoch CR

Finding the 3D geographic positions of **PS** is possible by installing a reference target for a period spanning multiple epochs, and measuring its position via GNSS. That way, the range and azimuth offsets are estimated as described above, while interferometry can be used to estimate the cross-range positions of points relative to the reference target, and the absolute cross-range position is anchored via the corner reflector. Fig. 4 shows the concept of the multi-epoch

method. The position of PS scatterers in the image (black symbols) is first corrected in the azimuth-range plane (gray). Then from the interferometric phase, the relative cross-range positions are computed (dashed). Finally, the known position of the CR reference point is used to determine the true geographic position of the point scatterers (hatched).

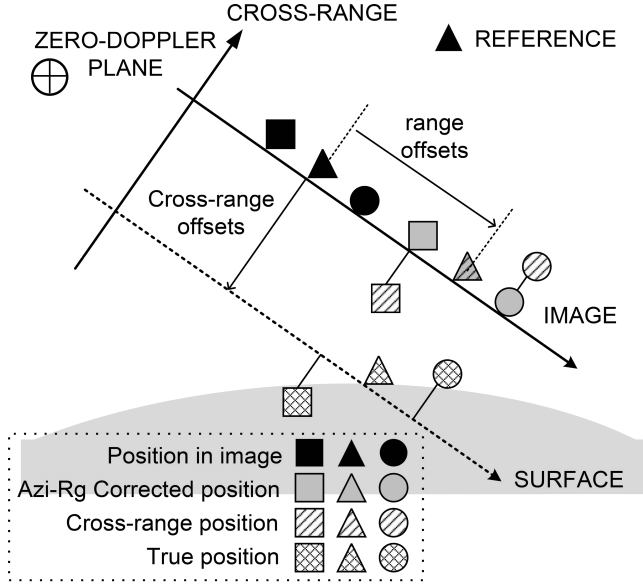


Figure 4: Multi-epoch approach: PS (black symbols) are first corrected for the offsets in an azimuth-range plane (gray symbols), and then differenced in cross-range via interferometry (dashed) and finally fixed for the cross-range offset (hatched symbols). The solid triangle indicates the reference point (GCP) for cross-range offset estimation.

The geographic elevation (cross-range) position $c_{cr,g}$ of the CR is derived from the GNSS-measured height $H_{cr,g}$ using Eq. (8). The offsets in azimuth and range direction are calculated from Eqs.(14) and (15), respectively. The variances of the calculated azimuth and range offsets are improved by the square root of the number of epochs n .

Since the CR persists for a long time it can be recognized as a PS. As such, the CR can be used as c_0 value in Eq. (4), i.e., $c_0 = c_{cr,g}$. The $\sigma_{cr,g}^2$ is dependent on the precision of the GNSS measurement and given by

$$\sigma_{cr,g}^2 = (\sigma_{e,g}^2 \cos^2 \alpha + \sigma_{n,g}^2 \sin^2 \alpha) \cos^2 \theta + \sigma_{u,g}^2 \sin^2 \theta. \quad (20)$$

The relative cross-range differences between the PS point cloud and the reference point is determined

using PS interferometry. The estimates of these relative differences will improve when more data will be used in the interferometric stack.

A stack of $n + 1$ acquisitions generates n independent pairs with different baselines $[B_{\perp,1}, \dots, B_{\perp,n}]^T$ and phase observations $[\phi_{T,1}, \dots, \phi_{T,n}]^T$ for target T , relative to the reference point. Using Eq.(4), the functional model with the initial range value of r_T^0 can be written as

$$y = E \left\{ \begin{bmatrix} \phi_{T,1} \\ \vdots \\ \phi_{T,n} \end{bmatrix} \right\} = \hat{G}_{n \times 1} \cdot c_T = \begin{bmatrix} -\frac{4\pi B_{\perp,1}}{\lambda r_T^0} \\ \vdots \\ -\frac{4\pi B_{\perp,n}}{\lambda r_T^0} \end{bmatrix} \cdot c_T. \quad (21)$$

The estimated cross-range is

$$\hat{c}_T = (G^T Q_y^{-1} G)^{-1} G^T Q_y^{-1} y, \quad (22)$$

and the variance is

$$\sigma_{\hat{c}_T}^2 = (G^T Q_y^{-1} G)^{-1}. \quad (23)$$

The covariance matrix Q_y of time series phase observations is a diagonal matrix with entries

$$[\sigma_{\phi_{T,1}}^2, \dots, \sigma_{\phi_{T,n}}^2]^T, \quad (24)$$

where σ_{ϕ} is the standard deviation of a single phase observation as described by (Dheenathayalan et al., 2017)

$$\sigma_{\phi} \approx \sqrt{\frac{2}{2SCR - \sqrt{3}/\pi}}. \quad (25)$$

Hereby, the precision of cross-range $\sigma_{\hat{c}_T}$ is

$$\sigma_{\hat{c}_T}^2 = \left(\frac{\lambda r_T^0}{4\pi} \right)^2 \cdot \left(\frac{B_{\perp,1}^2}{\sigma_{\phi_{T,1}}^2} + \dots + \frac{B_{\perp,n}^2}{\sigma_{\phi_{T,n}}^2} \right)^{-1}. \quad (26)$$

The precision of cross-range depends on the phase quality and the variability of the baseline. Longer baselines give a more precise cross-range estimation (Rocca, 2004) without requiring more data acquisitions.

Fig.5 shows the cross-range precision of a target with $SCR = 25$ dB as a function of the number of

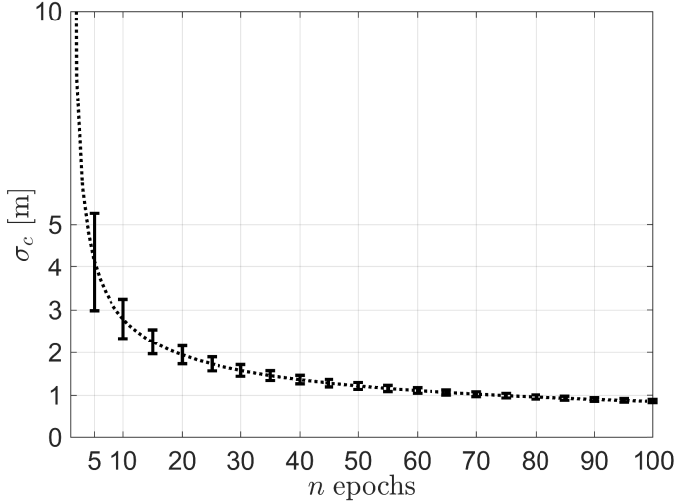


Figure 5: The standard deviation of estimated cross-range of a target with SCR 25 dB for Sentinel-1 as a function of the number of acquisitions n within an orbital tube with a radius of 100 m.

epochs n . The perpendicular baselines B_{\perp} were random values with uniform distribution at a range between -100m and 100m , which is the orbital tube of Sentinel-1 (Geudtner et al., 2017). The precision increases with the epochs, from about 1.7m with 25 epochs to better than 1m with 74 epochs or more.

4. DSM-assisted InSAR precise point positioning

A LiDAR-based DSM may be used as a network of thousands of GCPs. The precondition for the usage of a DSM for reference is that the LiDAR DSM and InSAR point cloud describe the same surface, or the penetration depth of LiDAR and SAR into the ground is equal. To fix the Δa , Δr , and c_0 of PSs, these PSs need to be matched with corresponding points in the LiDAR point cloud. We use the Iterative Closest Point method (ICP) with the PS positioning ellipsoids (Hanssen et al., 2018; Yang et al., 2019), which minimizes the differences between two clouds of points in an iterative way and generates transformation parameters.

We evaluate the positions of the LiDAR point cloud and the positions of the PS in the SAR geometry in the metric given by the covariance matrix. For this purpose, the LiDAR point cloud is radar-coded to the radar geometry using the orbit of the master image of the stack. The 3D position error ellipsoids, as defined by the positioning Variance-Covariance

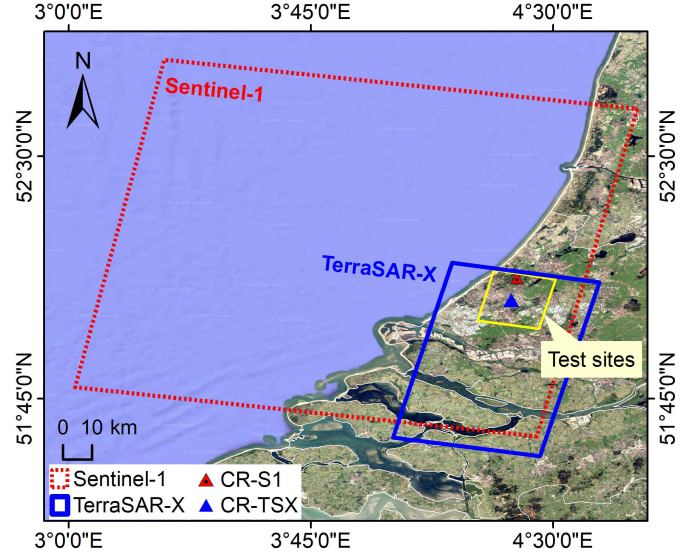


Figure 6: The coverage of TerraSAR-X and Sentinel-1 data and location of installed CRs.

(VC) matrices Q_{rac} of the PSs in 3D radar geometry (Dheenathayalan et al., 2016), with on the diagonal the variances $(\sigma_r^2, \sigma_a^2, \sigma_c^2)$ in range, azimuth and cross-range directions.

The transformation parameters estimated by the ICP method yield the offsets in azimuth, range, and cross-range, that we seek to correct. The quality of the corrected position is dependent on the quality of the DSM model and the accuracy of point registration.

5. Experiment setup

The TU Delft test sites are in Ypenburg and Wassenaar, the Netherlands. Two data-stacks were collected over this area. For each data stack, we processed at least 40 images. Fig. 6 shows the location of the test sites, outlines of the TerraSAR-X and Sentinel-1 data stacks, and the location of the installed reflectors. Tab. 1 provides the relevant parameters of the analyzed data. The PSI results from the two data stacks are different in point density, target detectability due to data characteristics variation.

At the Ypenburg test site, we installed six small (45cm sides) trihedrals, CR1–CR6, and one big (1m sides) trihedral, CR7. The CRs remained on the field between August 2012 and March 2014 and were optimally oriented for the geometry of the TerraSAR-X acquisitions. The reflectors are clearly visible in the

Table 1: TerraSAR-X, and Sentinel-1 SAR Data characteristics

Satellite/Parameter	TerraSAR-X	Sentinel-1
Test site	Ypenburg	Wassenaar
Track	T048	T110
Band	X	C
Start Date	2012.08.11	2017.11.08
End Date	2014.03.06	2018.07.18
Number of images	46	40
B_{\perp} [min/max] [m]	-382/142	-88.4/117.7
Acquisition mode	SM	IW
Pass direction	Desc	Desc
Polarization	HH	VV
Incidence angle [°]	22.3 – 25.6	35.7 – 41.7
Heading [°]	192.22	190.12
Rang. sampling [m]	0.9	2.3
Azim. sampling [m]	1.7	13.8
Rang. Bandw. [MHz]	150	56.5
Azim. Bandw. [Hz]	2765	327

mean intensity image of 46 TerraSAR-X images, as shown in Fig. 7.

For our analysis, we use CR4, CR5, CR6, and CR7 to avoid the impact of the mutual side-lobes of the first three. Differential GNSS and tachymetry are used to precisely measure the apex positions of these CRs. These positions are determined with a precision (1σ) of 1cm in the horizontal (east and north), and 2cm in the vertical.

In the Wassenaar site, we installed one square-based trihedral CR from February 2017, and two Double Back-flip (DBF) CRs (Hanssen, 2017) from November 2017, oriented for the Sentinel-1 descending data, see Fig. 8. The apex locations of these CRs are measured and calculated with one GNSS campaigns on 05-11-2017 with a precision of 1cm horizontally and 2cm vertically.

In addition to the CRs, we utilise a DSM model, AHN (*Actueel Hoogtebestand Nederland* in Dutch), collected over the Netherlands by means of airborne laser altimetry with a posting of 50cm (horizontally) for objects larger than 2×2 meters and a vertical offset uncertainty of 5cm and a 5cm stochastic error (Van der Zon, 2013; van Natijne et al., 2018). AHN is a multi-annual program, including AHN-1, AHN-2, AHN-3, providing both the raster data and the

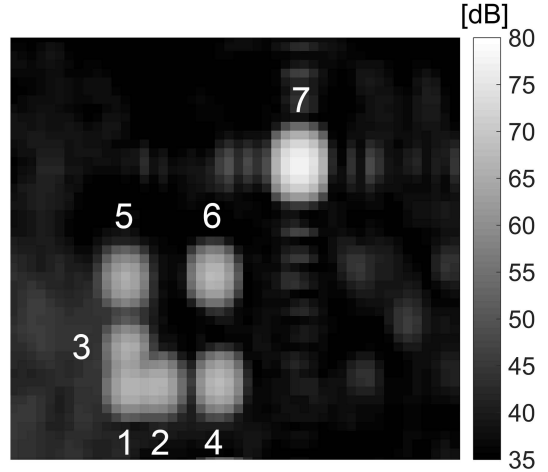


Figure 7: Mean intensity image from 46 TerraSAR-X images covering the seven corner reflectors at the Ypenburg test site.

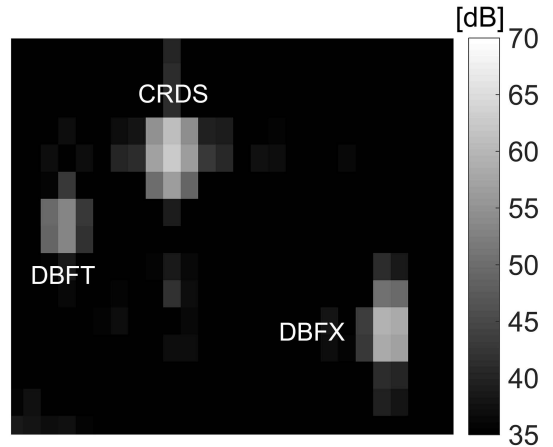


Figure 8: Mean intensity image from 40 Sentinel-1 images covering the three reflectors at the Wassenaar test site.

point clouds. We utilize the AHN-2 point cloud for DSM correction and the 0.5 meter grid DSM for cross-comparison.

6. Results

In this section, we present and compare the correction results of TerraSAR-X and Sentinel-1 data stack using the proposed methods. The SAR data-stacks were processed with the Delft implementation of Persistent Scatterer Interferometry (DePSI) (van Leijen, 2014).

6.1. TerraSAR-X results

Fig. 9 shows the estimated elevations for the PSs identified in the TerraSAR-X data stack. As usual,

Table 2: Calculated offsets in azimuth, range, and cross-range directions for the TerraSAR-X PSI point cloud.

Method	Δa [m]	Δr [m]	Δc_0 [m]
Single-epoch CR	0.52 ± 0.04	-2.25 ± 0.02	n/a
Multi-epoch CR	0.50 ± 0.01	-2.26 ± 0.02	20.40 ± 1.89
DSM	0.58 ± 0.04	-2.32 ± 0.04	19.01 ± 0.51
Geophysical ^a	0.57 ± 0.07	-2.28 ± 0.02	n/a

^a Correction includes azimuth shifting, path delay, solid earth tide, plate motion from Dheenathayalan et al. (2016).

high PS densities are found along streets and man-made structures. White areas correspond to vegetated areas and water bodies, where no PS was selected. The point density is 2141 PS/km². The results were projected in the Dutch national reference system RD (*'Rijksdriehoeksstelsel'* in Dutch) and vertical reference system NAP (*'Normaal Amsterdams Peil'* in Dutch). The estimated heights are color-coded, from -10 to 40m.

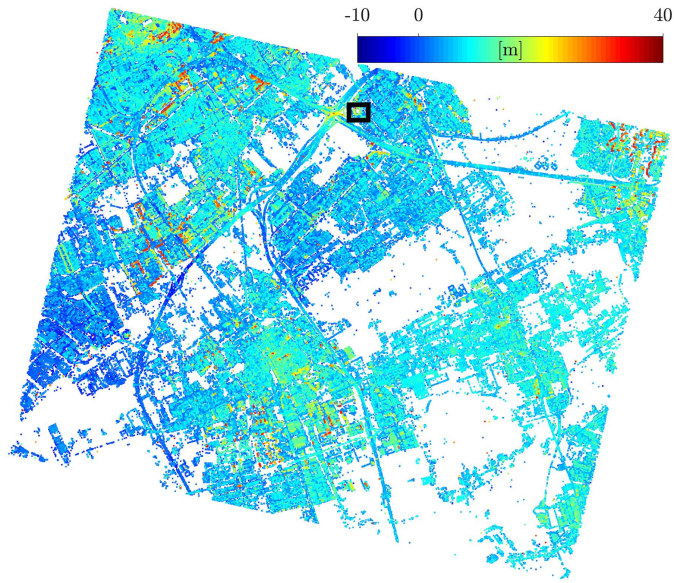


Figure 9: Geo-coded PSI point cloud for our test area generated from the TerraSAR-X data stack in RD coordinates. The x - and y - axes correspond to RD east and north, respectively. The estimated height is colour-coded in the NAP datum. The results in the Kyocera Stadium marked within a rectangular box were compared to the LiDAR point cloud in Fig. 10 and Fig. 11 .

Tab. 2 gives the offsets of the estimated positions of the CRs after applying the different correction methods with respect to their measured positions. The uncertainty of the CR-assisted approaches is calculated using Eqs. (16), (18), and (20), while the uncertainty of the sub-pixel localization is calculated according to the position variances of a target in a stack

of images. The performance of the DSM-assisted approach depends on the co-registration accuracy. It is calculated by dividing the LiDAR point cloud into several subsets, calculating the offsets respectively for each subset, and computing the variances of the resulting offsets.

The offsets estimated using the different approaches are similar, and consistent with the offsets estimated by Dheenathayalan et al. (2016). The largest offset was observed in the cross-range direction, which corresponds to the reference cross-range value. The atmospheric path delay mainly causes range offsets. Obviously, changing the coordinate system to a local geographic coordinate system introduces correlations between the different offsets. For example, a cross-range offset has components in both east and north directions.

The corrected positions were validated with the apex location measured with Differential GNSS and tachymetry for those CRs that were not used to estimate the corrections. The resulting Root Mean Square Errors (RMSE) in the radar coordinates (azimuth, range and cross-range), and local coordinates (east, north, and up) are reported in Tab. 3. Before the correction, the entire solution is tied to the height of a selected reference point. Similarly, we used the same height reference in the single-epoch approach and geophysical approach.

As expected, both single-epoch CR calibration and geophysical corrections do not correct for absolute cross-track errors, which results in coupled vertical and mostly east-west errors. Using a CR at all epochs, the offsets in elevation were compensated, achieving a decimeter-level 3D positioning error. The DSM-assisted corrections are similar to the multi-epoch CR correction for azimuth and range, but the cross range RMSE is twice as large: 2m instead of 1m.

Table 3: RMSE of CRs in the radar coordinates (azimuth, range and cross-range), and local coordinates (east, north, and up) for the TerraSAR-X point cloud. The geocoded position of PS before and after applying the corrections are compared with the apex location measured with GNSS in CRs. The post-correction methods includes single-epoch CR, multi-epoch CR, and DSM.

	a [m]	r [m]	c [m]	e [m]	n [m]	u [m]
Before Corrections	0.78	2.39	20.79	12.90	2.13	8.48
Single-epoch CR	0.31	0.18	20.79	7.59	0.46	8.48
Multi-epoch CR	0.32	0.17	1.01	0.67	0.36	0.41
DSM	0.28	0.13	2.01	1.60	0.31	0.81
Geophysical	0.28	0.16	20.79	7.54	0.41	8.48

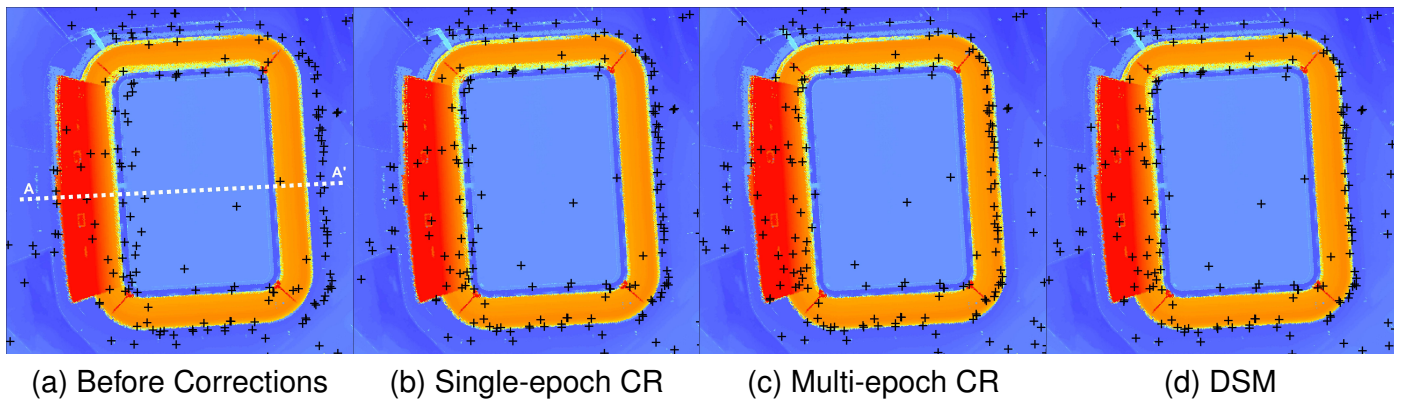


Figure 10: 2D horizontal accuracy analysis of the TerraSAR-X PS point cloud at the Kyocera Stadium. PS point cloud (a) before corrections, and corrected with (b) a single-epoch CR, (c) a multi-epoch CR, and (d) an airborne DSM model, overlaid on the LiDAR data. The LiDAR data is color-coded as Fig. 9. The 1D vertical analysis of Fig. 11 is along the line of AA'.

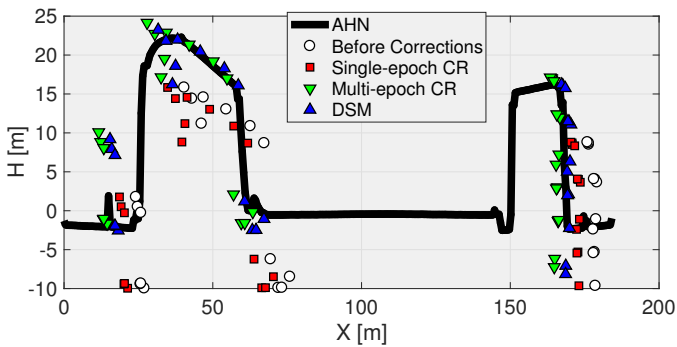


Figure 11: 1D vertical accuracy analysis of the TerraSAR-X PS point cloud over the Kyocera Stadium. PS point cloud before corrections, and point clouds corrected with a single-epoch CR, a multi-epoch CR, and an airborne DSM model, overlaid on the LiDAR data.

As a test of the geolocation, we compare the PS point cloud before and after correction to the reference LiDAR-based DSM for a region indicated by the rectangle in Fig. 9, which corresponds to a sports stadium in The Hague. Fig. 10 provides a top-view of the color-coded DSM with the PSs overlaid for the different methods. Before the corrections, there is a clear shift between the PSs and the stadium. The alignment improves after single-epoch CR correction, and it seems to enhance further using the multi-epoch and DSM-assisted approaches. Fig. 11 shows a cross section of the stadium along the AA' line indicated in Fig. 11. The multi-epoch CR and DSM corrections bring the points to the right height level.

6.2. Sentinel-1 results

The topographic map of PSI results from Sentinel-1 is illustrated in Fig. 12, projected in the RD-NAP reference system. The colors represent the estimated heights, from -10 to 140 m. The point density is 707 PS/km².

Table 4: Calculated offsets in azimuth, range, and cross-range directions for the Sentinel-1 point cloud.

	Δa [m]	Δr [m]	Δc_0 [m]
Single-epoch CR	16.41 ± 0.21	-1.09 ± 0.13	n/a
Multi-epoch CR	16.32 ± 0.03	-1.06 ± 0.03	-4.70 ± 1.81
DSM	14.48 ± 1.47	-0.96 ± 0.24	-2.63 ± 0.45

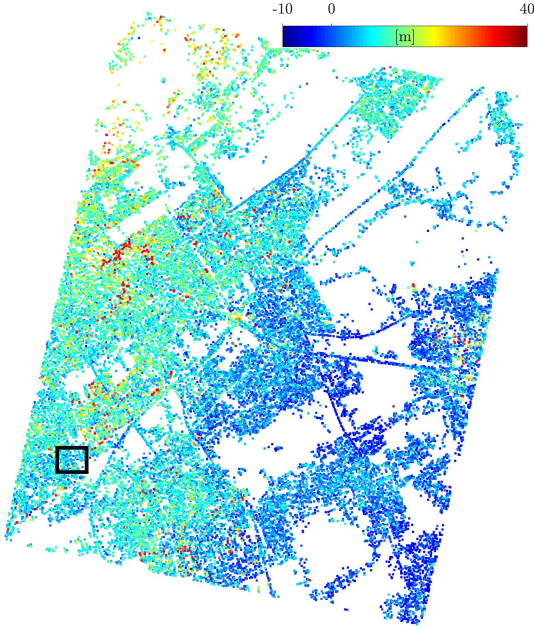


Figure 12: Geo-coded PSI point cloud for our test area generated from Sentinel-1 in RD coordinates. The x - and y - axes correspond to RD east and north. The estimated height is colour-coded in the NAP datum. The results in the Moerwijk area of the Hague, marked by the rectangular box, were compared to the LiDAR point cloud in Fig. 13 and Fig. 14.

Tab. 4 gives the offsets of the estimated positions of the CRs after applying the different correction methods. The largest offset was observed in the azimuth direction, followed by the elevation correction, and the range correction.

The azimuth offsets could be due to higher order bi-static effects, between the mid-scene bi-static correction and the required one due to the slant range offset from mid-scene, see Schubert et al. (2015). Recent research on the geolocation accuracy of Sentinel-1 data reports a subswath-dependent azimuth offset up to 4m in the IW mode (Schubert et al., 2017). Given the 20m azimuth resolution of Sentinel-1, the error is within the size of a resolution cell.

The 3D offsets estimated using the multi-epoch and DSM-assisted methods are roughly comparable,

although for range and azimuth direction the multi-epoch CR method is better, whereas for cross-range the DSM method is better, in terms of the variances. This is to be expected due to the coarse azimuth resolution of Sentinel-1, as the number of DSM points matched to a PS is drastically reduced.

The corrected positions were validated with GNSS measurements. The RMSE in the east, north, and up directions is given in Tab. 5. The 3D geolocation accuracy achieved using the multi-epoch method is approximately 3.6m. This is better than the absolute location error accuracy specification of Sentinel-1 (7m in 2D azimuth-range positioning) (Bourbigot et al., 2016). The geolocation accuracy obtained after a DSM-assisted correction is slightly worse but still better than the Sentinel-1 specifications. The corrected results assisted by single-epoch CR (about 5.4m) are also close to the specification. There is still about 3m of residual error in the north direction, which may relate to the azimuth errors reported by (Schubert et al., 2017).

The PS point cloud before and after the corrections is further compared with the reference LiDAR data. A zoom-in region is a group of buildings in the Hague, indicated by the rectangle in Fig. 12. Fig. 13 provides a top-view of the DSM data with the non-corrected and corrected PS point cloud. Clearly, the applied corrections have compensated for the 2D shift. The height shift was corrected with the single-epoch CR and the DSM-assisted method as the cross-section along the BB' line shows in Fig. 14.

6.3. DSM product evaluation

A DSM-assisted correction is a very appealing option, as it does not require the installation and maintenance of GCPs. However, the drawbacks of this approach is that it requires a non-trivial processing step to reliably match PS with points or features on the DSM. The accuracy of the estimated corrections, will, obviously, depend on the quality of the DSM.

Table 5: RMSE of CRs in the radar coordinates (azimuth, range and cross-range), and local coordinates (east, north, and up) for the Sentinel-1 point cloud. The geocoded position from PSI before and after applying the corrections are compared with the apex location measured with GNSS on the CRs. The post-correction methods includes a single-epoch CR, a multi-epoch CR, and DSM.

	a [m]	r [m]	c [m]	e [m]	n [m]	u [m]
Before Corrections	16.92	1.58	3.70	1.86	17.93	2.22
Single-epoch CR	3.80	0.74	3.70	3.47	3.63	2.22
Multi-epoch CR	3.80	0.67	1.62	0.72	3.46	0.97
DSM	4.26	0.74	1.45	1.13	4.29	0.88

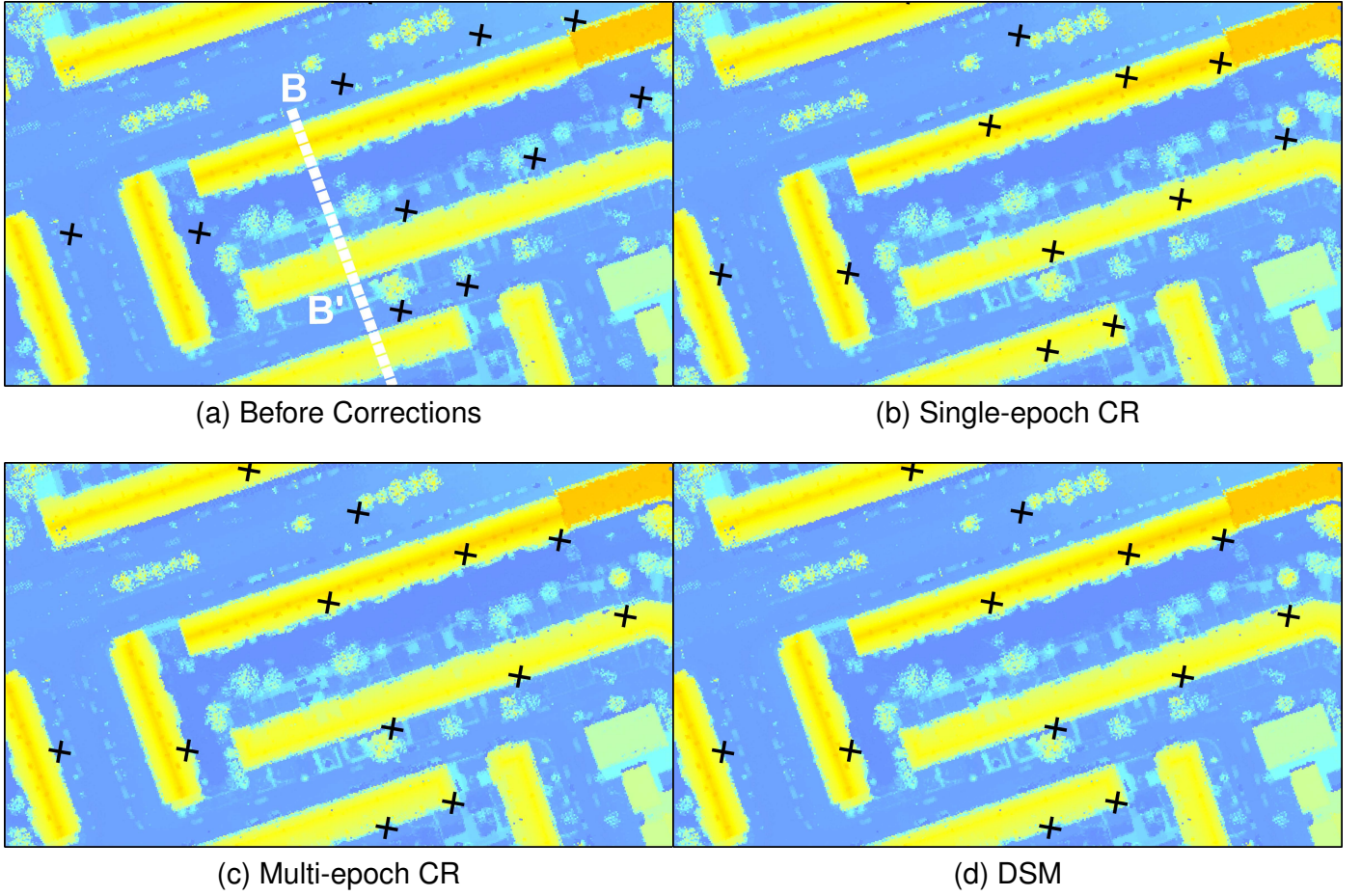


Figure 13: 2D horizontal accuracy analysis of Sentinel-1 PS point cloud of buildings in Moerwijk, the Hague. PS point cloud (a) before corrections, and corrected with (b) single-epoch CR, (c) multi-epoch CR, and (d) a airborne DSM model (DSM), overlaid on the LiDAR data. The LiDAR data is color-coded as Fig. 12. The 1D vertical analysis is along the line of AA', see Fig. 14.

A standard product specification for digital elevation model named as Digital Terrain Elevation Data (DTED) is released by National Geospatial-Intelligence Agency (NGA) with the definitions of absolute positioning accuracy and spatial resolution for each level, specifically DTED-1 and DTED-2 (Heady et al., 2009; Zink et al., 2006). The DTED was defined for globe scale elevation data, and the higher level data is referring

to as High-Resolution Terrain Information (HRTI). The DTED-3/4 is also called HRTI-3/4. Therefore, we analyze the positioning precision given varying DTED levels, see Tab.6.

The quality of the LiDAR DSM data used in this study (AHN-2) is significantly better than DTED-4 specification. In order to evaluate the DSM quality dependence of the DSM method, we degraded the

Table 6: Digital Terrain Elevation Model (DTED) and High-Resolution Terrain Information (HRTI) specifications.

Specification	Spatial Resolution	Absolute vertical Accuracy (90%)	Absolute Horizontal Accuracy (90%)
DTED-1	90 m (3 arcsec)	50	30
DTED-2	30 m (1 arcsec)	23	18
DTED-3/HRTI-3	12 m (0.4 arcsec)	10	10
DTED-4/HRTI-4	6 m (0.2 arcsec)	5	5

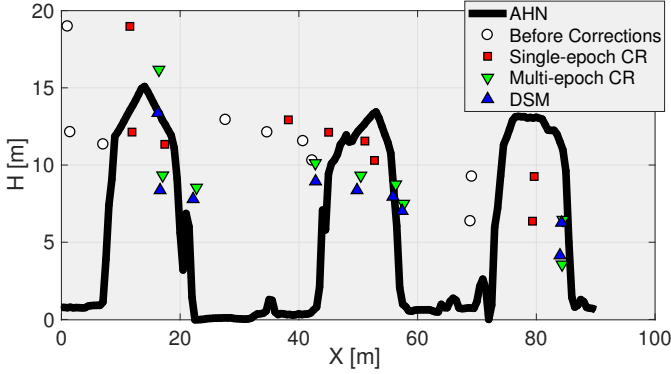


Figure 14: 1D vertical accuracy analysis of Sentinel-1 PS point cloud in Moerwijk, the Hague. PS point cloud before corrections, point clouds corrected with single epoch CR, multi-epoch CR, and a airborne DSM model, overlaid on the LiDAR data.

AHN-2 to match the different DTED specifications by filtering the data spatially to the desired resolution and adding zero-mean Gaussian distributed noise.

Fig. 15 shows the positioning precision as a function of the DTED level. The vertical axis shows the 3D Positioning Dilution of Precision (PDOP) as

$$\text{PDOP} = \sqrt{\text{RMSE}_c^2 + \text{RMSE}_n^2 + \text{RMSE}_u^2}, \quad (27)$$

where RMSE is the root mean square error with respect to GNSS measurements of the apex location of CRs.

For a DSM at DTED1 level, the PDOP values are close to the values before corrections, implying that this DSM product does not improve the geolocation of PS point clouds. For DTED2, the PDOP values improve, but not significantly. A significant improvement was observed moving to DTED3 levels. This is due to the fact that the spatial resolution of DTED3 is closer to that of Sentinel-1. The precisions achieved using DTED4 are yet better, and the LiDAR-based AHN data yield the best results. This is due to the dense spatial sampling and precise absolute position-

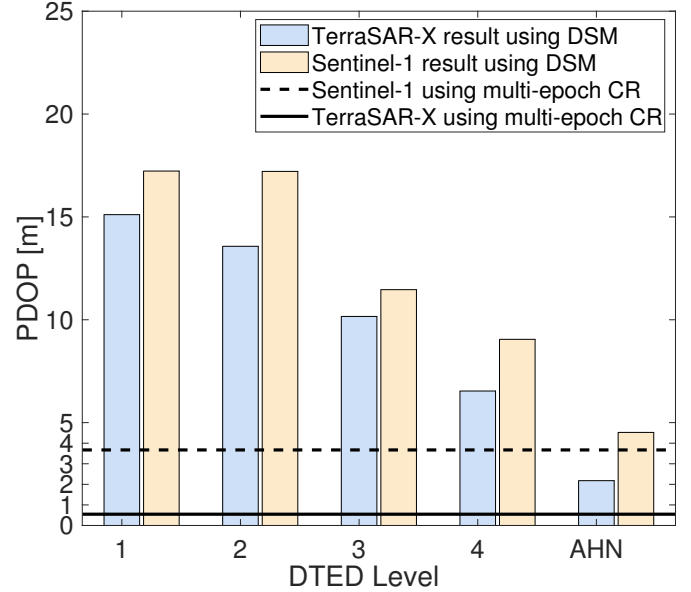


Figure 15: Positioning precision as a function of the DTED level.

ing of AHN data for depicting the height variability within the imaging scene.

The result of the DSM-assisted geolocation approach depends on the precision of the available DSM and also the used algorithm, see examples using different algorithms with DSM to evaluate the height shift between PSI point cloud and DSM in Chang & Hanssen (2014); Yang et al. (2016).

7. Discussion

The practical pros and cons of the discussed methods for precise point positioning are summarized in Tab. 7. We define σ_{CR} as the precision of the calculated offsets of the single epoch CR approach, T_0 as the estimated time required for the installation of a single CR monumentation, and n as the number of epochs. Note that T_0 depends on local conditions, typically ranging from 0.5 to 3 days.

Table 7: The characteristics of the positioning correction methods. Advantages and disadvantages.

Methods	Single-epoch CR	Multi-epoch CR	DSM	Geophysical
Solution space	Line (2D)	Point (3D)	Point (3D)	Line (2D)
Advantages	Temporary deployment; ad hoc; No monumentation needed; Fast (10^3); easy; cheap	3D correction Highest 3D precision	3D corrections No area access necessary	No area access necessary
Disadvantages	2D bias correction only; No elevation correction; Requires area access;	Monumentation needed; Permanent deployment; Requires area access; Regular inspection and maintenance needed; Expensive; Resources	Requires high quality DSM; Requires significant height variability; Requires high quality point matching method	2D bias correction only; No elevation correction; Requires model input for atmosphere, tides, tectonics, instrument;
Effort	1 CR placement; 1 GNSS real time kinematic;	1 CR monumentation: T_0 [†] ; 1 GNSS real time kinematic; Regular check-up required	Algorithmic	Computation
Precision	σ_{CR} [†]	σ_{CR}/\sqrt{n} [†]	dm	dm

[†] σ_{CR} : precision of the calculated offsets in the Single-epoch CR approach. T_0 : estimated time required for the installment of a single CR monumentation. n : the number of epochs.

Both the single-epoch calibration as well as the geophysical correction lack the absolute cross-range correction, which yields only limited improvement in positioning accuracy. Of these two, the former requires physical access to the area, while the latter needs various physical parameters to be available.

The best accuracy and precision is achieved using one CR over multiple epochs. The maintenance cost scales with the number of epochs, which is dependent on the baseline distribution of the SAR data stack: a greater number of epochs is needed if the orbital tube is smaller.

The DSM-assisted approach is less accurate than the multi-epoch method, but it is a reasonable alternative if a high-precision DSM is available, with the main advantage of not requiring area access.

8. Conclusions

The geolocalization of PSI point clouds significantly improves their overall practical value. As this requires a mapping from 2D radar coordinates to 3D geographic coordinates, GCP's such as corner reflectors can assist in this mapping. The optimal way of deploying a corner reflector is by deploying it in a time series of SAR images, such that its phase can be analyzed as a persistent scatter. That way, the highest reliability, precision, and accuracy in the geolocalization of a PSI point cloud is obtained. Yet, this comes at a cost in terms of efforts and resources. Alternatively, when a high-precision, high resolution digital surface model is available, DTED4-level or better, exhibiting sufficient elevation variability, this could be used as a virtual set of GCPs, almost comparable geolocalization precision.

Deployment of a corner reflector for just one single SAR acquisition, or using additional geophysical information does not yield compensate absolute 3D geographic coordinates, and can only be used to limit the degrees of freedom in azimuth-range plane.

Acknowledgment

The authors would like to thank the constructive comments of the anonymous reviewers. We appreciate the GNSS measurements provided by Dr. Hans van der Marel. This work was supported by the National Natural Science Foundation of China under Grant 41571435. Financial support provided to M. Yang by the China Scholarship Council (CSC) during the study in Delft is acknowledged.

References

- Balss, U., Gisinger, C., & Eineder, M. (2018). Measurements on the absolute 2-D and 3-D localization accuracy of TerraSAR-X. *Remote Sensing*, *10*.
- Bamler, R., & Eineder, M. (2005). Accuracy of differential shift estimation by correlation and split-bandwidth interferometry for wideband and delta-k SAR systems. *IEEE Geosci. Remote Sens. Lett.*, *2*, 151–155.
- Bourbigot, M., Johnson, H., & Piantanida, R. (2016). *Sentinel-1 Product Definition*. MDA Document Number: SEN-RS-52-7440 MacDonald, Dettwiler and Associates Ltd.: Richmond, BC, Canada (esa cdr1 number: pd11-1, pd12-1 ed.).
- Chang, L., & Hanssen, R. F. (2014). Detection of cavity migration and sinkhole risk using radar interferometric time series. *Remote Sens. Environ.*, *147*, 56–64.
- Cong, X., Balss, U., Eineder, M., & Fritz, T. (2012). Imaging geodesy - centimeter-level ranging accuracy with TerraSAR-X: An update. *IEEE Geosci. Remote Sens. Lett.*, *9*, 948–952.
- Crosetto, M., Monserrat, O., Cuevas-Gonzalez, M., Devanthy, N., & Crippa, B. (2016). Persistent scatterer interferometry: A review. *ISPRS J. Photogramm. Remote Sens.*, *115*, 78–89.
- Dheenathayalan, P., Caro Cuenca, M., Hoogeboom, P., & Hanssen, R. F. (2017). Small reflectors for ground motion monitoring with InSAR. *IEEE Trans. Geosci. Remote Sens.*, *55*, 6703–6712.
- Dheenathayalan, P., Small, D., Schubert, A., & Hanssen, R. (2016). High-precision positioning of radar scatterers. *J. Geod.*, (pp. 403–422).
- Duque, S., Parizzi, A., Zan, F. D., & Eineder, M. (2016). Precise and automatic 3d absolute geolocation of targets using only two long-aperture SAR acquisitions. In *2016 IEEE International Geoscience and Remote Sensing Symposium (IGARSS)* (pp. 7415–7418).
- Eineder, M., Minet, C., Steigenberger, P., Cong, X., & Fritz, T. (2011). Imaging Geodesy - toward centimeter-level ranging accuracy with TerraSAR-X. *IEEE Trans. Geosci. Remote Sens.*, *49*, 661–671.
- Ferretti, A., Savio, G., Barzaghi, R., Borghi, A., Musazzi, S., Novali, F., Prati, C., & Rocca, F. (2007). Submillimeter accuracy of InSAR time series: Experimental validation. *IEEE Trans. Geosci. Remote Sens.*, *45*, 1142–1153.
- Garthwaite, M. C. (2017). On the design of radar corner reflectors for deformation monitoring in multi-frequency InSAR. *Remote Sens.*, *9*, 648.
- Gernhardt, S., Auer, S., & Eder, K. (2015). Persistent scatterers at building facades-evaluation of appearance and localization accuracy. *ISPRS J. Photogramm. Remote Sens.*, *100*, 92–105.
- Gernhardt, S., Cong, X., Eineder, M., Hinz, S., & Bamler, R. (2012). Geometrical fusion of multitrack ps point clouds. *IEEE Geosci. Remote Sens. Lett.*, *9*, 38–42.
- Geudtner, D., Prats, P., Yaguemartinez, N., De Zan, F., Breit, H., Larsen, Y., Monti-Guarnieri, A., Barat, I., Navas-Traver, I., & Torres, R. (2017). Sentinel-1 constellation SAR interferometry performance verification. In *ESA Fringe 2017* (pp. 1457–1460).
- Gisinger, C., Balss, U., Pail, R., Zhu, X. X., Montazeri, S., Gernhardt, S., & Eineder, M. (2015). Precise three-dimensional stereo localization of corner reflectors and persistent scatterers with TerraSAR-X. *IEEE Trans. Geosci. Remote Sens.*, *53*, 1782–1802.
- Hanssen, R. (2017). A radar retroreflector device and a method of preparing a radar retroreflector device. URL: <https://patents.google.com/patent/W02018236215A1/en> international Patent WO2018236215A1.
- Hanssen, R. F. (2001). *Radar Interferometry: Data Interpretation and Error Analysis*. Dordrecht: Kluwer Academic Publishers.
- Hanssen, R. F., Van Natijne, A., Lindenbergh, R. C., Dheenathayalan, P., Yang, M., Chang, L., Van Leijen, F. J., Lopezdekker, P., Der Maaden, J. V., Van Oosterom, P. et al. (2018). Scatterer identification and analysis using combined InSAR and laser data. *The EGU General Assembly*, .
- Heady, B., Kroenung, G., & Rodarmel, C. (2009). High resolution elevation data (hre) specification overview. In *ASPRS/MAPPS 2009 Conference, San Antonio, Texas*.
- van Leijen, F. (2014). *Persistent Scatterer Interferometry based on Geodetic Estimation Theory*. Netherlands Geodetic Commission, The Netherlands.
- Marinkovic, P., Ketelaar, G., van Leijen, F., & Hanssen, R. (2008). InSAR quality control: Analysis of five years of corner reflector time series. In *in Proceedings of the 5th International Workshop on ERS/Envisat SAR Interferometry (FRINGE '07)*.
- Miranda, N., Rosich, B., Meadows, P., Haria, K., Small, D., Schubert, A., Lavallo, M., Collard, F., Johnsen, H., Monti-Guarnieri, A., & D’Aria, D. (2013). The Envisat ASAR mission: A look back at 10 years of operation. In *Esa Living Planet Symposium*. ESA.
- Montazeri, S., Rodriguez Gonzalez, F., & Zhu, X. X. (2018). Geocoding error correction for InSAR point clouds. *Remote*

- Sens.*, 10.
- van Natijne, A. L., Lindenbergh, R. C., & Hanssen, R. F. (2018). Massive linking of PS-InSAR deformations to a national airborne laser point cloud. *ISPRS - International Archives of the Photogrammetry, Remote Sensing and Spatial Information Sciences, XLII-2*, 1137–1144.
- Olmsted, C. (1993). Alaska SAR facility scientific SAR user's guide. *Alaska SAR Facility Technical Report ASF-SD-003*, .
- Rocca, F. (2004). Diameters of the orbital tubes in long-term interferometric SAR surveys. *IEEE Geosci. Remote Sens. Lett.*, 1, 224 – 227. doi:10.1109/LGRS.2004.830125.
- Sarabandi, K., & Chiu, T.-C. (1996). Optimum corner reflectors for calibration of imaging radars. *IEEE Trans. Antennas Propag.*, 44, 1348–1361.
- Schreier, G. (Ed.) (1993). *SAR Geocoding: data and systems*. Karlsruhe: Wichmann Verlag.
- Schubert, A., Jehle, M., Small, D., & Meier, E. (2010). Influence of atmospheric path delay on the absolute geolocation accuracy of TerraSAR-X high-resolution products. *IEEE Trans. Geosci. Remote Sens.*, 48, 751–758.
- Schubert, A., Miranda, N., Geudtner, D., & Small, D. (2017). Sentinel-1A/B combined product geolocation accuracy. *Remote Sens.*, 9, 607.
- Schubert, A., Small, D., Miranda, N., Geudtner, D., & Meier, E. (2015). Sentinel-1A product geolocation accuracy: Commissioning phase results. *Remote Sens.*, 7, 9431–9449.
- Shimada, M., Isoguchi, O., Tadono, T., & Isono, K. (2009). PALSAR radiometric and geometric calibration. *IEEE Trans. Geosci. Remote Sens.*, 47, 3915–3932.
- Small, D., Rosich, B., Meier, E., & Nüesch, D. (2004). Geometric calibration and validation of ASAR imagery. In *CEOS WGCV SAR Calibration & Validation Workshop* (p. 8). Ulm Germany.
- Small, D., Schubert, A., Rosich, B., & Meier, E. (2007). Geometric and radiometric correction of ESA SAR products. In *ESA ENVISAT Symposium* (p. 6). Montreux, Switzerland: Citeseer.
- Stein, S. (1981). Algorithms for ambiguity function processing. *IEEE Trans. Acoust., Speech, Signal Processing*, 29, 588–599.
- Xia, Y., Kaufmann, H., & Guo, X. (2002). Differential SAR interferometry using corner reflectors. In *Geoscience and Remote Sensing Symposium, 2002. IGARSS '02. 2002 IEEE International* (pp. 1243–1246 vol.2).
- Yang, M., Dheenathayalan, P., Chang, L., Wang, J., Lindenbergh, R., Liao, M., & Hanssen, R. (2016). High-precision 3d geolocation of persistent scatterers with one single-epoch GCP and LIDAR DSM data. In L. Ouwehand (Ed.), *Proceedings of Living Planet Symposium 2016* (pp. 398–398). Netherlands: European Space Agency volume SP-740 of *European Space Agency (ESA-SP)*.
- Yang, M., López-Dekker, P., Dheenathayalan, P., Biljecki, F., Liao, M., & Hanssen, R. F. (2019). Linking persistent scatterers to the built environment using ray tracing on urban models. *IEEE Trans. Geosci. Remote Sens.*, 57, 5764–5776.
- Zhang, L., Balz, T., & Liao, M. (2012). Satellite SAR geocoding with refined rpc model. *ISPRS J. Photogramm. Remote Sens.*, 69, 37 – 49.
- Zhu, X. X., Montazeri, S., Gisinger, C., Hanssen, R. F., & Bamler, R. (2016). Geodetic SAR tomography. *IEEE Trans. Geosci. Remote Sens.*, 54, 18–35.
- Zink, M., Fiedler, H., Hajnsek, I., Krieger, G., Moreira, A., & Werner, M. (2006). The tandem-x mission concept. In *2006 IEEE International Symposium on Geoscience and Remote Sensing* (pp. 1938–1941).
- Van der Zon, N. (2013). *Kwaliteitsdocument Actueel Hoogtebestand Nederland AHN2*. Technical Report the Netherlands: HetWaterschapshuis. In Dutch.
- van Zyl, J. J. (1990). Calibration of polarimetric radar images using only image parameters and trihedral corner reflector responses. *IEEE Trans. Geosci. Remote Sens.*, 28, 337–348.